Comparison of Different Subgrid-Scale Models of Large Eddy Simulation for Indoor Airflow Modeling

Mingde Su
Senior Post-Doctoral Fellow, Building Technology Program, Massachusetts Institute of Technology, Cambridge, MA 02139-4307

Qingyan Chen[*]
Associate Professor, Building Technology Program, Massachusetts Institute of Technology, Cambridge, MA 02139-4307, Phone: (617) 253-7714, Fax: (617) 253-6152, Email: qchen@mit.edu

Che-Ming Chiang
Professor
Department of Architecture, National Cheng-Kung University, Tainan, 701, Taiwan

The Smagorinsky subgrid-scale model, a dynamic subgrid-scale model, and a stimulated subgrid-scale model have been used in a large eddy simulation (LES) program to compute airflow in a room. A fast Fourier transformation (FFT) method and a conventional iteration method were used in solving the Poisson equation. The predicted distributions of indoor air velocity, temperature, and contaminant concentrations show that the three subgrid-scale models can produce acceptable results for indoor environment design. The dynamic and stimulated models performed slightly better than the Smagorinsky model. The use of FFT can significantly reduce the computing time. LES is a tool of the next generation of indoor air distribution design.

1. Introduction

Computational Fluid Dynamics (CFD) can be used to determine turbulent fluid flow, heat transfer, and the transport of chemical species for indoor environment design, allowing for the determination of thermal comfort parameters and indoor air quality (Chen [1]). The numerical simulation of turbulent flow in an indoor space can be divided into three types: direct numerical simulation (DNS), Reynolds Averaged Navier-Stokes (RANS) equation modeling, and Large Eddy Simulation (LES).

DNS solves the Navier–Stokes equations for flow motion numerically without using a turbulence model, producing a very reliable simulation. Turbulent flow consists of vortices with various scales, where the ratio between the largest scale and the smallest scale is approximately equal to $Re^{3/4}$ (Lesieur [2]). In order to describe the various scales of the vortices, the grid number used to solve turbulent flow should be larger than $Re^{9/4}$. Since the Reynolds number for a typical indoor airflow is 10^4, the grid number required is on the order of one billion. Currently, a super-computer is capable of handling a grid number of up to 10^8. If such a large-capacity computer necessary for modeling indoor airflow were to become available, the computing time required to reach a useful solution would be a few months. It is therefore impractical at the present time to use DNS as a tool for indoor environment design.

Most of the current indoor airflow designs solve the RANS equations, because this numerical simulation can be performed on a PC. Since the RANS equations require a coarse grid system and calculate averaged flow properties (air velocity, temperature, and species concentrations, etc.), the computing time required is only a few hours for most indoor

environment designs. However, the RANS equations contain unknown Reynolds stresses that have to be modeled by a turbulence model. At present, no generic turbulence models are available. Most of the developed turbulence models, such as the mixing length theory, one-equation models, two-equations models, and second moment models, may perform reasonably well in one case, but poorly in another [1]. Therefore, the accuracy of the numerical results is not guaranteed, and the designers have difficulties in choosing a suitable turbulence model. In addition, RANS equation modeling cannot provide instantaneous information concerning turbulent flows, which is important for thermal comfort design. Therefore, RANS modeling has severe limitations in building environmental design.

LES divides flow motion into two parts: large-scale and small-scale motions. LES directly calculates large-scale motions. Small-scale motions, with sizes normally smaller than the numerical grid size, are modeled with subgrid scale models. When the grid size is sufficiently small, the impact from the subgrid scale models on the flow motion will be small. Furthermore, the subgrid scale models will become general, because the turbulent flow at very small scales is nearly isotropic. Therefore, the subgrid scale models generally contain fewer empirical coefficients and artificial factors than those used in the turbulence models of the RANS equations. Since the flow information at small scales may not be important for engineering applications, LES is becoming an important and powerful tool in studying turbulence (Piomelli [3], Lesieur and Metais [4]). However, questions still remain as to how accurate LES is, and how much computing time LES requires for indoor environment design. The accuracy is related to the approximations used in the subgrid scale models, while the computing time is influenced by the numerical technique used in solving the transport equations.

Various subgrid scale models have been developed in the last twenty years. Most of them are eddy viscosity models, which use the Boussinesq hypothesis to calculate eddy viscosity. The most popular models used in engineering can be mainly divided into the Smagorinsky model and the dynamic models. Our study focuses on these two types of eddy-viscosity subgrid scale models as well as on one non-eddy viscosity model. The Smagorinsky model uses a constant eddy viscosity coefficient for the entire flow domain. This model is not suitable for complex flows, where the coefficient may vary over time and location. The dynamic models calculate the eddy viscosity coefficient according to local flow characteristics. The dynamic models are more appropriate than the Smagorinsky model. On the other hand, Shah and Ferziger [5] developed a non-eddy viscosity model, the stimulated small-scale subgrid (SSSS) model, which calculates small-scale motion by using a stimulated method based on the operation. Since this model has a strong mathematical and physical background, it deserves further attention. However, performing LES needs more demanding time than RANS modeling.

Among the computing time used by LES, solving the Poisson equation with the conventional iteration method would consume 90% of the time. In order to reduce the computing cost, the fast Fourier transformation (FFT) method is used. In the present paper, the FFT method is used for both periodic and Neumann boundary conditions.

The effort of this investigation is to systematically examine the performance of the Smagorinsky sub-grid scale (SSGS) model (Smagorinsky [6]), the Dynamic Sub-Grid Scale (DSGS) model (Germano et al. [7]), and the SSSS model for indoor airflow simulation. This investigation also compares the computing time required by the conventional iteration method and by the FFT method to solve the Poisson equation.

2. Governing Equations and Subgrid Scale Models

Using a spatial filter, LES divides turbulence flow into large-scale and small-scale (grid-scale) motions. The filtered flow parameters for large-scale motions can be obtained by solving the following filtered Navier-Stokes equations:

$$\left.\begin{aligned}
&\frac{\partial \overline{\upsilon}_i}{\partial x_i} = 0 \\[6pt]
&\frac{\partial \overline{\upsilon}_i}{\partial t} + \frac{\partial \overline{\upsilon}_i \overline{\upsilon}_j}{\partial x_j} = -\frac{1}{\rho}\frac{\partial p}{\partial x_i} + \nu \frac{\partial^2 \overline{\upsilon}_i}{\partial x_i \partial x_j} - \frac{\partial \tau_{ij}}{\partial x_i} \\[6pt]
&\frac{\partial \overline{T}}{\partial t} + \frac{\partial \overline{T}\overline{\upsilon}_i}{\partial x_i} = \kappa \frac{\partial^2 \overline{T}}{\partial x_i \partial x_j} - \frac{\partial T_{Tj}}{\partial x_i} \\[6pt]
&\frac{\partial \overline{C}}{\partial t} + \frac{\partial \overline{C}\overline{\upsilon}_i}{\partial x_i} = \kappa_c \frac{\partial^2 \overline{C}}{\partial x_i \partial x_j} - \frac{\partial D_{Cj}}{\partial x_i} + q_c
\end{aligned}\right\} \tag{1}$$

where

$$\tau_{ij} = \overline{\upsilon_i \upsilon_j} - \overline{\upsilon}_i \overline{\upsilon}_j \tag{2}$$

$$T_{Ti} = \overline{T\upsilon_i} - \overline{T}\overline{\upsilon}_i \tag{3}$$

$$D_{Ci} = \overline{C\upsilon_i} - \overline{C}\overline{\upsilon}_i \tag{4}$$

The variables, τ_{ij}, T_{Tj}, and D_{Cj}, are unknown, and should be calculated by subgrid scale models. This study uses three subgrid scale models, the SSGS, DSGS, and SSSS models, in order to compare their performance for indoor airflow simulation. The following section discusses how τ_{ij} is modeled. The same concept can be applied to T_{Tj}, and D_{Cj}.

2.1 Eddy-viscosity models. The SSGS and DSGS models are eddy viscosity models that have a common form:

$$\tau_{ij} - \frac{\delta_{ij}}{3}\tau_{kk} = -2\nu_T \overline{S}_{ij} \quad \text{with} \quad S_{ij} = \frac{1}{2}\left(\overline{\upsilon}_{i,j} + \overline{\upsilon}_{j,i}\right) \tag{5}$$

The eddy-viscosity models are used to determine the eddy-viscosity, ν_T. Using the equilibrium assumption (that the turbulence in a grid with small scale eddies is in equilibrium, and the dissipated energy is implemented from the large scale eddies), the following algebraic model can be used to calculate the eddy-viscosity:

$$\nu_T = C_M \Delta^2 |\overline{S}| \overline{S}_{ij}, \quad |\overline{S}| = \left(2\overline{S}_{ij}\overline{S}_{ij}\right)^{1/2} \tag{6}$$

where Δ is the grid scale and is equal to the cubic root of a cell volume, if the grid cell is anisotropic. C_M is a parameter in the model. The SSGS and DSGS models are separately discussed below.

a) Smagorinsky subgrid-scale model (SSGS): The widely used Smagorinsky model is the simplest subgrid-scale model. The model uses $C_M = C_s^2$, where C_s is the Smagorinsky coefficient. Normally, C_s is a constant in the range of $0.12 - 0.2$. This coefficient must be

decreased (Piomelli et al. [8]) for shear flows (e.g. flows near solid boundaries or transitional flows) by using the van Driest damping function or the intermittency function.

b) Dynamic subgrid-scale model (DSGS): Although the ad hoc modification on the Smagorinsky coefficient can be used for transitional and turbulent flows, Germano et al. [7] concluded that it is impossible to find a single, universal constant for different flows. In some cases, the ad hoc modifications are far from desirable. In addition, the Smagorinsky model cannot account for the energy transfer from small-scale eddies to large-scale eddies (backscatter), which can be significant in many flows. The development of the DSGS model reflects significant progress in the subgrid-scale modeling of non-equilibrium flows. The DSGS model calculates the model coefficient from the energy of the smallest resolved scale, rather than by setting a priori parameters like the Smagorinsky model.

The DSGS model defines a grid filtering scale, $\overline{\Delta}$, and a test filtering scale, $\widetilde{\Delta}$ (Germano et al. [7]). Two filtering functions, $\overline{G}$ and $\widetilde{G}$, are used over $\overline{\Delta}$ and $\widetilde{\Delta}$, respectively. By applying $\widetilde{\overline{G}}$ $(= \widetilde{G}\overline{G})$ to the Navier-Stokes equations, the subgrid scale stresses on the test filter can be obtained as:

$$T_{ij} = \overline{\widetilde{\upsilon_i \upsilon_j}} - \widetilde{\upsilon}_i \widetilde{\upsilon}_j \tag{7}$$

The first term on the right side of Eq. (7) cannot be directly determined, like the one in Eq. (2). However, by applying the basic assumptions of eddy viscosity models, the following is true:

$$\tau_{ij} - \frac{\delta_{ij}}{3}\tau_{kk} \cong m_{ij} = -2\,C\,\overline{\Delta}^2\,\left|\overline{S}\right|\,\overline{S}_{ij}$$

$$T_{ij} - \frac{\delta_{ij}}{3}T_{kk} \cong M_{ij} = -2\,C\,\widetilde{\Delta}^2\,\left|\widetilde{\overline{S}}\right|\,\widetilde{\overline{S}}_{ij} \tag{8}$$

where C is the same for both filters. As a result, the following is obtained:

$$L_{ij}\overline{S}_{ij} \equiv (T_{ij} - \widetilde{\tau}_{ij})\overline{S}_{ij} = -2C\left(\widetilde{\Delta}^2\left|\widetilde{\overline{S}}\right|\widetilde{\overline{S}}_{ij}\overline{S}_{ij} - \overline{\Delta}^2\left|\overline{S}\right|\overline{S}_{ij}\overline{S}_{ij}\right) \tag{9}$$

Averaging the equation along a homogeneous or periodical direction of the flow produces

$$C = -\frac{1}{2}\frac{\left\langle L_{ij}\overline{S}_{ij}\right\rangle}{\left\langle \widetilde{\Delta}^2\left|\widetilde{\overline{S}}\right|\widetilde{\overline{S}}_{ij}\overline{S}_{ij} - \overline{\Delta}^2\left|\overline{S}\right|\overline{S}_{ij}\overline{S}_{ij}\right\rangle} \tag{10}$$

The symbol $\langle\rangle$ stands for an average over the homogeneous or periodical direction. Therefore, the model is only suitable for homogeneous turbulence. Lilly [9] suggested that the coefficient can be determined by the least square method. This method uses the following equation as an object function:

$$Q = \left(2CM_{ij} - \left(\widetilde{\Delta}^2\left|\widetilde{\overline{S}}\right|\widetilde{\overline{S}}_{ij}\overline{S}_{ij} - \overline{\Delta}^2\left|\overline{S}\right|\overline{S}_{ij}\overline{S}_{ij}\right)\right)^2 \equiv \left(2CM_{ij} - L_{ij}\right)^2 \tag{11}$$

From this, the optimal coefficient becomes

$$C = \frac{L_{ij}M_{ij}}{2M_{ij}M_{ij}} \tag{12}$$

The DSGS model can be applied to various turbulent flows. For better numerical stability, it is necessary to smooth the C distribution (Zhang and Chen [10]), and set C to be greater than zero. Since the backscatter can only be described with a negative C, there is a contradiction between the backscatter and the numerical stability.

2.2 Non-eddy viscosity model. By filtering, LES divides unfiltered flow parameters, such as velocity, pressure, temperature, and species concentrations, into resolved (large-scale) parameters and unresolved (small-scale) parameters. A non-eddy viscosity model attempts to obtain the unresolved parameters by using mathematical and/or physical methods based on statistical theory or DNS data. With both the large-scale and small-scale velocities known, the Reynolds stress can be calculated.

A simple method used to generate the unfiltered parameter distribution is the Taylor expansion series. By letting u^* stand for $u(x)$ at x_i, and $u'(x) = u(x) - \overline{u}(x)$ (refer to Figure 1), the Taylor expansion produces

$$u(x) = u_i^* + (x - x_i)\left(\frac{d\,u}{d\,x}\right)_i^* + \frac{(x - x_i)^2}{2}\left(\frac{d^2 u}{d\,x^2}\right)_i^* + \cdots\cdots \tag{13}$$

By neglecting the third-order and higher-order terms and replacing the derivatives with central differencing ones, this equation becomes

$$u(x) = u_i^* + (x - x_i)\frac{u_{i+1}^* - u_{i-1}^*}{2h} + \frac{(x - x_i)^2}{2}\frac{u_{i+1}^* - 2u_i^* + u_{i-1}^*}{h^2} \tag{14}$$

By filtering $u(x)$ over 2Δ through the use of a box-filter, the filtered velocity is:

$$\overline{u}_i = u_i^* + \frac{\Delta^2}{6}\frac{u_{i+1}^* - 2u_i^* + u_{i-1}^*}{h^2} \tag{15}$$

Then, by letting $\Delta = h/2$,

$$\overline{u}_i = \frac{u_{i+1}^*}{24} + \frac{11\,u_i^*}{12} + \frac{u_{i-1}^*}{24} \tag{16}$$

For a non-uniform grid distribution, this equation becomes

$$\overline{u}_i = au_{i-1}^* + bu_i^* + cu_{i+1}^* \tag{17}$$

where

$$a = \frac{h_i^2(m^2 - 3m) + h_i h_{i-1}(3m - m^2) + h_{i-1}^2 m^2}{12 h_{i-1}(h_i + h_{i-1})}, \quad m = \frac{\Delta_i + \Delta_{i-1}}{h_i + h_{i-1}}$$

$$b = 1 - a - c$$

$$c = \frac{h_i^2 m^2 + h_i h_{i-1}(3m - m^2) + h_{i-1}^2(m^2 - 3m)}{12 h_{i-1}(h_i + h_{i-1})}$$

(18)

with $h_i = x_{i+1} - x_i$. This can then be rewritten in a simple operator form:

$$L_x(u_i^*) = \bar{u}_i$$

(19)

For a three-dimensional case,

$$L(u_{i,j,k}^*) = \bar{u}_{i,j,k} \qquad L = L_x L_y L_z$$

(20)

The Reynolds stresses can then be calculated from

$$\tau_{ij} = \overline{u_i^* u_j^*} - \overline{u_i^*}\,\overline{u_j^*}$$

(23)

This model is identical to the SSSS model developed by Shah and Ferziger [5]. This paper has mathematically explained the SSSS model. In addition, T_{Ti} and D_{Ci} can be determined with the same method. The procedure to calculate the Reynolds stresses and other second order correlations are as follows (let f and g be two variables where f can be a velocity component [u, v, or w] while g can be a velocity component, temperature, or species concentration):

a) Calculate f^* and g^* from $\bar{f}$ and $\bar{g}$, respectively, at all interior cells by using Eq. (20). This procedure solves a series of tri-diagonal algebraic equation systems in the x-, y- and z-directions. Since, according to Eq. (18), the coefficients in every row satisfy a + b + c = 1, the tri-diagonal coefficient matrix of the operator L_x is non-singular, and there are no instability problems.
b) Determine the product $f^* g^*$ at all the interior cells.
c) Compute $\overline{f^* g^*}$ by using Eq. (17). This is a series of simple algorithm operations.
d) Calculate $\overline{f^* g^*} - \overline{f^*}\,\overline{g^*}$ in order to obtain the Reynolds stresses and other correlations.

In the implementation of the SSSS model, we solve a series of tri-diagonal equation systems and complete simple arithmetic operations. It does not demand more computing time than the DSGS models.

3. Numerical Method

3.1 Difference scheme in time and space. The present investigation studied indoor airflows, which have relatively low Reynolds numbers. The numerical oscillation or instability is not significant. However, this oscillation or instability can be problematic when simulating airflow around buildings. A solution to avoid this problem is the use of the third

order upwind scheme for the convection terms. Since numerical instability was not significant for this indoor airflow study, the second order Adams-Bashforth scheme was used.

3.2 Projection method. The equations that need to be solved numerically for indoor airflow are the continuity, momentum, energy, and species concentration equations. The indoor air can be considered to be incompressible. The buoyancy resulting from air density variations produced by a temperature difference is added to the momentum equation via the Boussinesq assumption. The continuity equation of incompressible flow has no derivative term over time and cannot be directly solved simultaneously with the momentum equation. In the projection method (Chorin [11]), however, the continuity and momentum equations can be related through pressure. The projection method is described below.

The filtered Navier-Stokes equations are written in following form:

$$\left. \begin{array}{l} \dfrac{\partial\, \overline{\upsilon}_i}{\partial\, x_i} = 0 \\[4mm] \dfrac{\partial\, \overline{\upsilon}_i}{\partial\, t} + \overline{\upsilon}_j \dfrac{\partial\, \overline{\upsilon}_i}{\partial\, x_j} = -\dfrac{1}{\rho}\dfrac{\partial\, p}{\partial\, x_i} + \dfrac{\partial}{\partial\, x_j}\left(\nu\dfrac{\partial\, \overline{\upsilon}_i}{\partial\, x_j} + \tau_{ij} \right) \end{array} \right\} \tag{24}$$

The projection method solves the momentum equation without the pressure term:

$$\dfrac{\partial\, \overline{\upsilon}_i^*}{\partial\, t} + \overline{\upsilon}_j^* \dfrac{\partial\, \overline{\upsilon}_i^*}{\partial\, x_j} = \dfrac{\partial}{\partial\, x_j}\left(\nu\dfrac{\partial\, \overline{\upsilon}_i^*}{\partial\, x_j} + \tau_{ij} \right) \tag{25}$$

where $\overline{\upsilon}_i^*$ is the predicted velocity. The predicted velocity does not normally satisfy the continuity equation. However, by using a pressure correction, the predicted velocity can be modified to obtain the true velocity. A Poisson equation of pressure can be established by subtracting Eq. (25) from the momentum equation, Eq. (24). Then, by taking the divergence of both sides of the obtained equation, and by considering the continuity equation, we obtain a Poisson equation of pressure:

$$\dfrac{1}{\Delta t}\dfrac{\partial\, \overline{\upsilon}_i}{\partial\, x_i} = -\dfrac{1}{\rho}\dfrac{\partial^2 p}{\partial\, x_i \partial\, x_i} \tag{26}$$

By solving this Poisson equation, we obtain the pressure p, which is used to modify the predicted velocity using the following equation:

$$\overline{\upsilon}_i^{n+1} = \overline{\upsilon}_i^* - \dfrac{1}{\rho}\Delta t \dfrac{\partial\, p}{\partial\, x_i} \tag{27}$$

This modified velocity now satisfies the continuity equation, and is therefore the true velocity.

When applying the Fourier transformation to the Navier-Stokes equations, the pressure term is translated in the direction normal to the velocity plane. Therefore, ignoring the pressure term in the physical space is equivalent to projecting the Navier-Stokes equations onto the velocity plane in the spectral space. This is the reason this method is called the projection method (Lesieur [2]).

3.3 Differencing scheme. In order to numerically solve the partial differential equations, the present study uses the staggered grid system and the second order central-differencing scheme. For the time term, this investigation uses the second order Adams-Bashforth scheme.

3.4 Poisson equation and its solvers. If the Poisson equation were to be solved by the iteration method, it would consume about 90% of the overall computing time. Therefore, it is very important to develop an efficient solver for the Poisson equation. The present study uses FFT to improve the efficiency, accuracy, and speed of solving the Poisson equation.

FFT is used in both periodic and Neumann boundary conditions. In the case of Neumann boundary conditions, the Gauss-Chebyshev transformation is found to be acceptable. After reorganizing the coefficients (Su [12]), FFT can also be used in place of the discrete Gauss-Chebyshev transformations without decreasing the accuracy and efficiency. In the presented numerical examples, a non-uniform grid system is allowed in only one direction when using the FFT method to solve the Poisson equation of pressure.

Note that if all boundary conditions for the pressure are either periodic or homogeneous Neumann ones, the Poisson equation will have either no solution, or multiple solutions due to the singularity of the differencing-equation system. To ensure a unique solution, the sum of $q_{i,j,k}$ in the differencing equations over i = 1, 2, …, IM, j = 1, 2, …, JM, and k = 1, 2, …, KM should be zero (or should have a numerical error less than 10^{-6}). The pressure at a reference point or the average pressure in the whole flow domain should be set to zero.

When the flow domain contains obstacles in a room, such as occupants, computers, and furniture, the above-mentioned methods cannot be directly used due to the no-flux conditions on the surfaces of these obstacles. Therefore, it is necessary to ensure that the normal velocity at the surfaces, υ_n, be equal to zero. The present study introduces an additional term, $-\beta\upsilon_n - \alpha\upsilon_n |\upsilon_n|$, into the momentum equation at the surfaces (McGrattan et al. [13], Peskin [14], Goldstein et al [15]):

$$\frac{\partial \upsilon_n}{\partial t} + \text{Conv} = -\frac{1}{\rho}\frac{\partial p}{\partial n} + \text{Diss} - \beta\upsilon_n - \alpha\upsilon_n |\upsilon_n| \tag{34}$$

Note that $\frac{\partial \upsilon_n}{\partial t} = -\beta\upsilon_n - \alpha\upsilon_n |\upsilon_n|$ is an ordinary differential equation. When solving this ordinary differential equation, υ_n will quickly approach a small value if $\beta > 0$ and $\alpha > 0$ (this study uses $0.8/\Delta t$ for β and 10 for α). Therefore, the additional term seems to be a damping term and Eq. (34) can be approximated as:

$$\text{Conv} = -\frac{1}{\rho}\frac{\partial p}{\partial n} + \text{Diss} \tag{35}$$

This approach is used at the obstacle surfaces for all three components of velocity. In fact, this method exploits the relatively small changes in pressure from one time step to the next in order to enforce the no-flux condition on the obstacle surfaces, because the pressure at the current time step is unknown until the Poisson equation is solved.

Our experience shows that υ_n changes from 10^{-4} to 10^{-6} very quickly, and remains unchanged afterwards. Since υ_n is normally several orders smaller than the mean velocity in the flow domain, υ_n can be considered to be zero, which implies a successful simulation of a solid surface. This approximation method does not need to specify pressure boundary conditions on an obstacle surface, and the corresponding grids can be treated as a normal internal one. Therefore, the Poisson equation can still be solved by using the above-mentioned FFT algorithm.

4. Results

The above-mentioned subgrid scale models and numerical algorithms have been used to study indoor airflow. Indoor airflow consists of forced convection, natural convection, and mixed convection (which is a combination of forced and natural convection). This section will examine the performance of the subgrid scale models in predicting these three convection flows in a room.

4.1 Forced Convection. This study used forced convection flow in a room with measured air velocity profiles from Restivo [16]. The room geometry is shown in Figure 2, where H = 3 m. The velocity at the inlet was uniform and equal to 0.455 m/s. The flow Reynolds number was 5000, based on the inlet height and air velocity. The inlet height was 0.168 m. The air velocity was measured by a laser Doppler anemometer.

The computations used a uniform air velocity profile at the inlet, and a zero gradient condition for the air velocity at the outlet. Our computation applied a uniform mean velocity profile using six points across the jet. This was rather inconsistent with the experimental data. The experiment measured a small perturbation, which was neglected in the computation. All of these considerations were added in the revision. The log-law wall function was used for the walls (Wilcox [19]). The computational meshes employed were 66x18x34 and 66x34x34 corresponding to the length (x), height (y), and width (z) directions. The grid distribution was uniform in the x and z directions, and non-uniform in the y direction. The numerical results show a very small difference between the two meshes as compared in Figure 4. The results in this paper are from the finer mesh, for t = 400 to 800 s. Figure 3 shows the computed airflow pattern. Aside from the large vortex in the center of the room, there was a small eddy in the upper right corner, which was observed in the experiment.

The dimensionless time step used in this calculation was $\Delta t = 0.01$ s, which was much larger than the 0.002 s time step normally used for the iteration method in solving the Poisson equation. Therefore, the high accuracy of the FFT algorithm greatly improved the numerical stability.

Figure 4 compares the computed mean dimensionless air velocity ($U = u/u_{in}$) and the computed dimensionless velocity fluctuation (u_r = [mean square-root fluctuate velocity in x direction]/u_{in}) with the corresponding experimental data from the middle section of the room at both x = H and 2H. The Smagorinsky coefficient used in the SSGS model was 0.16, which was recommended for indoor airflow by Murakami [17]. The results show that the DSGS and SSSS models performed slightly better than the SSGS model in calculating the mean air velocity. The under-prediction by the SSGS model may be attributed to the large viscosity computed. The calculated air velocities by the DSGS and the SSSS models are almost identical. The DSGS model calculated the turbulence viscosity coefficient according to the local flow type, and the SSSS model calculated the quasi-Reynolds stress by using the stimulated small-scale velocity. Therefore, these two models described the flow better than the SSGS model. For velocity fluctuations, none of the three models produced satisfactory

results. The SSGS model generally under-predicted the velocity fluctuation, while the other two models over-predicted this velocity fluctuation in the area near the air inlet. The discrepancies among the results of the three models are large in the area where there is a large gradient in mean velocity. The SSSS model computed the small-scale velocity according to the mean velocity gradient. The larger the mean velocity gradient is, the higher the stimulated small-scale velocity becomes. Therefore, the velocity fluctuation was also high.

Table 1 compares the computational time used by the conventional iteration method with the time used by the FFT method for the case with a total grid number of 130x34x34. These computations were carried out on an Alpha workstation and a Cray-T90 supercomputer. The results produced from the Cray supercomputer show that the FFT method is ten times faster than the iteration method. When comparing the FFT method results between the Alpha workstation and the Cray supercomputer, the computing time per time step per grid cell was 2×10^{-5} s on the workstation, and 8×10^{-6} s on the single-processor supercomputer. However, for the iteration method results, it was 6×10^{-4} s on the workstation, and 8×10^{-5} s on the supercomputer. Since FFT uses double precision on the workstation, the computing speed of the FFT method is only three times faster than the iteration method. Since double precision is default on the supercomputer, computation with the FFT can reduce the computing time more significantly than that with the iteration method.

4.2 Natural Convection. This investigation also studied natural convection flow in a cavity, as shown in Figure 5. Cheesewright et al. [18] measured the air velocity, temperature, and turbulent energy in the cavity. Their experimental data were used to compare with our numerical results. The cavity was 2.5 m high, 0.5 m wide, and 0.5 m deep. The left wall was heated to 68.0°C, and the right wall was kept at 22.2°C. All the other walls were insulated. Cheesewright et al. [18] noted that the cavity was not well insulated.

The computations used only one non-uniform grid distribution in the x-direction. This non-uniform grid distribution is very important in obtaining the correct results, due to the sharp temperature gradient near the hot and cold walls. However, a limited computer memory prevented the use of a uniform grid system in x-direction since this would require many grids. The smallest grid size close to the walls in the x-direction was only 0.005 m. The y- and z-directions used uniform grids, since the air velocity, temperature, and turbulent kinetic energy varied only slightly in these two directions, as shown in Figure 5. Periodic boundary conditions were applied in the z-direction. In addition, the computation used the Boussinesq approximation to consider the buoyancy effect. Surprisingly, two grid meshes (34x34x18 and 66x66x34) used in the computations yielded the same results. Figure 5 shows the computed mean airflow pattern and air temperature distribution in the middle section of the cavity, using the finer grid mesh. The air temperature distribution is given for the dimensionless temperature, T, which is defined as $T = (t - t_c)/(t_h - t_c)$. In order to identify the impact of the grid scale and the wall function on the mean flow distribution, this investigation used two different wall functions: the one-layer log-law wall function (1L), and the two-layer wall function (2L) from Wilcox [19]. Our results do not show any significant difference between these two wall functions.

Figure 6 compares the computed mean profiles of air velocity, turbulent kinetic energy, and air temperature with the measured data at the mid-height of the cavity. In Figure 6, the units of velocity and turbulent kinetic energy are m/s and m^2/s^2, respectively. In the LES simulations with the DSGS model, both wall functions were used.

The results confirm that the three models produced similar mean air velocity and temperature profiles. These results show that the wall functions had a small influence on the profiles of mean temperature and velocity. The notable difference was found in the vicinity of the walls, seen in the velocity and turbulent kinetic energy profiles of Figure 6. The mean

velocity values calculated in the vicinity of the hot and cold walls were much greater than the measured data, although the grid scale was very small, and the computations used both wall functions. It seems that there are some unknown reasons influencing the values of velocity in this region. Further investigation is therefore necessary. In addition, Figure 6(b) shows that the turbulent kinetic energy values obtained by the DSGS model in the vicinity of the wall were greater than the measured data. However, these values were closer to the measured data in all other regions than those results obtained by the SSGS and SSSS models. From these results, it can be concluded that the damping of the DSGS model is smaller than that of the SSGS and SSSS models. Therefore, the results of the DSGS model were the best among the three subgrid scale models.

The computed mean air temperature was much higher than the experimental data. The reason for this discrepancy is that the poor insulation used in the cavity led to a significant heat loss in the experiment. This condition also induced the asymmetry of the measured mean air velocity. Therefore, the measured data was not asymmetric due to the poor insulation on the cavity, and it was incorrect.

4.3 Mixed convection. The mixed convection study used a displacement ventilation case that supplied cold air through the diffuser in the lower part of a room, and exhausted warm air at the ceiling level, as shown in Figure 7. This is a practical case of ventilation system design for a room. The room was 5.16 m long, 3.65 m wide, and 2.43 m high. This case presents a real scenario of a two-person office with many heated and unheated objects, such as the occupants, lighting, computers, and furniture. Yuan et al. [20] measured the air temperature, air velocity, and tracer-gas (SF_6) concentration for the case. The tracer-gas was used to simulate CO_2 emissions from the two occupants. The temperature of the inlet airflow from the diffuser was $t_{sup} = 17.0^{\circ}C$, and the ventilation rate was 183 m^3/h. The total heat sources in the room were 636 W. The measured data were used here to validate the LES results.

According to the studies of forced and natural convection cases, a very fine grid resolution did not provide more accurate results. The coarse grid distributions are acceptable for engineering applications. In addition, this mixed convection case had smaller temperature and velocity gradients in the flow domain so that it did not need a very fine grid resolution. Hence, the current study used a grid distribution of 66x46x34. The grid is quite coarse for such a complex geometry. The grid distribution is non-uniform in the y-direction, and uniform in the other two directions. The time step used was 0.005 s over a 300 s period. With such a grid resolution and time step, it is possible to calculate the mixed convection case on an Alpha workstation with a single 21264 processor. The total computing time was about 30 hours.

The boundary conditions used in the study were as follows. The log-law wall functions were used for all the solid surfaces. The thermal boundary conditions for the surfaces were set as either fixed temperatures or heat fluxes. At the air supply inlet, a uniform velocity and temperature profile was assumed and the turbulence intensity was estimated to be 10%. The boundary conditions for the exhaust were zero pressure and zero gradient for all other variables.

Figure 8 shows the mean and instantaneous airflow pattern at the middle section of the office. The cold air from the diffuser moved downwards rapidly along the floor due to the buoyancy effect. The mean airflow pattern showed a large and weak recirculation in the lower part of the room. In the upper part of the room, there were some areas of recirculation caused by the thermal plumes from the heated objects, such as the computers, occupants, and overhead lights. The airflow pattern computed was similar to that observed with the smoke visualization (Yuan et al. [20]).

The computed results shown in Figure 8 illustrate a significant difference between the

mean and instantaneous flow patterns. The instantaneous flow is unstable, and the flow appears to be very chaotic. This phenomenon can be found in another cross section through the computer, as shown in Figure 9. Note that the velocity fluctuation in the office can be very high, even though the mean velocity is very small. This is especially evident in the upper part of the room. This information, which is normally not available from turbulence modeling, is very important for thermal comfort design.

In addition, the experiment has also measured the mean air velocity with omni-directional anemometers. Figure 10 compares the computed mean air velocity with the experimental data at five locations in the office. Y/H = 0 corresponds to the floor surface, and Y/H = 1 to the ceiling surface. The bottom right figure shows a floor plan where the five measuring locations are labeled. The experiment observed a low frequency oscillation (2-5 minutes per cycle). The data were averaged in the measurements over a period of a few seconds. Therefore, the experimental data appears rather smooth. The three subgrid-scale models of LES predicted very similar velocity distributions, except in the area close to the floor at location 6. This difference can be attributed to the constant coefficient used in the Smagorinsky model. Since the anemometers are not suitable for low velocity measurements, the comparison is not conclusive. Nevertheless, the trend and the magnitude of the velocity distributions are the same between the computed results and the measured data.

Figure 11 shows the profiles of the mean air temperature at the five positions in the room. All the computed results agree well with the experimental data. The differences among the three subgrid-scale models are generally small, although the SSSS model seems to perform the best. The SSSS model estimated the small-scale temperature from the heat fluxes and the temperature distribution. Since the temperature variation over time and location was found to be not significant, these results suggest that the air temperature is not very sensitive to the turbulence viscosity.

One important objective in studying indoor airflow is to predict contaminant concentration distributions. Carbon dioxide is often considered to be a contaminant. The experiment conducted by Yuan et al. [20] used tracer-gas to simulate the carbon dioxide from the two occupants. Figure 12 presents the computed tracer-gas concentration distributions and the corresponding experimental data at five different positions in the room. The agreement between the experimental data and computational results is poor. This is because the diffusion process is very slow for this case. The average of the results should be made over a long period of time in order to obtain more accurate mean results. Our calculation for a total of 500 s is too short. Nevertheless, the three subgrid-scale models are able to predict the trend and magnitude of the concentration distributions.

5. Conclusion

This investigation used three subgrid-scale models of LES to study forced, natural, and mixed convection flows in a room. The three subgrid-scale models are the Smagorinsky (SSGS) model, a dynamic model (DSGS), and a stimulated small-scale SGS (SSSS) model (also referred to as the deconvolution model in some literature, such as [21]). The LES used fast Fourier transformation (FFT) as its numerical algorithm. The experimental data from the three cases are used to validate the numerical results. This study leads to the following conclusions:

1) The SSGS, DSGS, and SSSS models can be used for the prediction of indoor airflow. The performance of the DSGS and SSSS models was slightly better than that of the SSGS model. The differences between the DSGS and SSSS models are small. For building design, the LES models produce results with reasonable accuracy.

2) Because the SSSS model has a solid mathematical and physical background, it deserves further attention. In the present paper, the use of this model has been extended through the LES calculation of temperature and concentration.

3) The LES provides not only the mean flow parameters, but also instantaneous airflow information. The instantaneous flow information is an important thermal comfort parameter, and it cannot be easily obtained through turbulence modeling. Therefore, LES is a promising tool for the next generation of building environmental design.

All results show that the computational profiles of velocity and turbulent kinetic energy in the vicinity of the wall are far different from the measured data. Therefore, further investigation of this problem is necessary.

Nomenclature

a	coefficient in the difference Poisson equation	S	source
a,b,c	coefficients of stimulated operator. See Eq. (18)	Q	Object function
C	species concentration; coefficient of dynamic model	q_c	Source term of concentration
C_M	parameter in the eddy-viscosity model	S	tensor of deformation rate
C_s	Smagorinsky coefficient	S_{ij}	Component of $S, = \frac{1}{2}\left(\overline{\upsilon}_{i,j} + \overline{\upsilon}_{j,i}\right)$
Conv	convection term in the momentum equation	T	dimensionless temperature
D_{Cj}	$\overline{C\upsilon_i} - \overline{C}\,\overline{\upsilon}_i$ species concentration flux	T_{Tj}	$= \overline{T\upsilon_i} - \overline{T}\,\overline{\upsilon}_i$ heat flux
Diss	dissipation term in the momentum equation	T_{ij}	$\overset{\sim}{\overline{\upsilon_i\upsilon_j}} - \widetilde{\overline{\upsilon}}_i\widetilde{\overline{\upsilon}}_j$
G	filtering function	T_{kk}	$\displaystyle\sum_{i=1}^{3} T_{ii}$
H	height	t	time; temperature
h_i	$= x_{i+1} - x_i$	U	dimensionless mean velocity
h	for the case of uniform grid	u	a general flow parameter; component of velocity in x direction
I	Unit matrix	u_r	dimensionless fluctuate velocity
IM,JM,KM	total numbers of nodes in the x-, y-, and z-directions	$u(x)$	A function of x
n	normal direction	u_i^*	value of $u(x)$ at x_i
$\overset{\circ}{i}$	$\sqrt{-1}$	$\overline{u}(x)$	filtered function of $u(x)$
L_{ij}	$= T_{ij} - \widetilde{\tau}_{ij}$	$u'(x)$	$= u(x) - \overline{u}(x)$
$L_x; L_y; L_z$	stimulated operator in the x-, y-, and z-directions	$\overline{u}_i$	value of $\overline{u}(x)$ at x_i

L	$= L_x L_y L_z$		v	component of velocity in y direction; scale of velocity
L_{ij}	$= T_{ij} - \widetilde{\tau}_{ij}$		$\overline{\upsilon}_i$, $\overline{\upsilon}_j$	velocity components in the x_i- and x_j-directions
M_{ij}	$= T_{ij} - \dfrac{\delta_{ij}}{3} T_{kk} = -2\,C\,\widetilde{\overline{\Delta}}^2 \left|\widetilde{\overline{S}}\right| \widetilde{\overline{S}}_{ij}$		$\overline{\upsilon}_{i,j}$	$= \partial \overline{\upsilon}_i / \partial x_j$
m	See Eq. (18)		x_i	x coordinate of i-th node; $x_1 = x;\ x_2 = y;\ x_3 = z$
m_{ij}	$= \tau_{ij} - \dfrac{\delta_{ij}}{3} \tau_{kk} = -2\,C\,\overline{\Delta}^2 \left|\overline{S}\right| \overline{S}_{ij}$		x, y, z	Cartesian coordinates
p	pressure			

Greek letters

$\alpha,\ \beta$	selected parameters in Eq. (39)		κ_c	species diffusivity
Δ	grid scale, filtering scale		ρ	air density
Δt	time step		ν	Kinetic viscosity of fluid
δ_{ij}	Kronecker symbol, if i=j, it is 1, else 0.		ν_T	eddy-viscosity
κ	thermal diffusivity		τ_{ij}	Reynolds stresses

Subscripts

c	cold wall		m,n	indexes in the x-, y- phase space
e	environment		n	normal component
exh	exhaust		s	supply or source
h	hot wall			
i	component in x_i direction			

Superscripts

*	value of original function at node (see Figure 1.); imaginative velocity in projection method		$\overline{(\ )}$, $\overset{\sim}{(\ )}$	filtered value with scale $\overline{\Delta}$ and $\widetilde{\Delta}$
n	time level		$(\ )'$	small scale value

Kevin McGrattan of the National Institute of Standard and Technology for many useful discussions.

References

[1] Chen, Q., 1997, "Computational fluid dynamics for HVAC: successes and failures," ASHRAE Transactions, **103**, Part 1, pp. 178-187.

[2] Lesieur, M., 1997, *Turbulence in Fluids* (third revised and enlarged edition), Kluwer Academic Publishers, Dordrecht.

[3] Piomelli, U., 1999, " Large Eddy simulation: achievements and challenges," Progress in Aerospace Sciences, **35**, pp. 335-362.

[4] Lesieur, M., and Metais, O., 1996, "New trends in large eddy simulations of turbulence," Annual Review of Fluid Mech., **28**, pp. 45-82.

[5] Shah, K. B., and Ferziger, J. H., 1995, "A new non-eddy viscosity subgrid-scale model and its application to channel flow," Center for Turbulence Research Annual Research Briefs.

[6] Smagorinsky, J., 1963, "General circulation experimental with the primitive equations," Mon. Weather Rev., **91**, pp. 99-164.

[7] Germano, M., Piomelli, U., Moin, P., and Cabot, W.H., 1991, "A dynamic subgrid-scale eddy viscosity model," Phys. Fluids **A**, **3**, pp. 1760-64.

[8] Piomelli, U., Cabot, W.H., Moin, P., and Lee, S., 1991, "Subgrid scale backscatter in turbulent and transitional flows," Phys. Fluids **A**, **3**(11), pp. 1766-71.

[9] Lilly, D.K., 1992, "A proposed modification of the Germano subgrid-scale closure method," Phys. Fluids **A**, **4**(3), pp. 633 – 635.

[10] Zhang, W., and Chen, Q., 2000, "Large eddy simulation of natural and mixed convection airflow indoors with two simple filtered dynamic subgrid scale models," Numerical Heat Transfer Part A: Applications, **37**(5), pp. 447-463.

[11] Chorin, A.J., 1968, "Numerical solution of incompressible flow problem," in Studies in *Numerical Analysis* 2, Society for Industrial and Applied Mathematics, Philadelphia, Pennsylvania, pp. 64-70

[12] Su, M.D., 1993, "LES of turbulent flow in straight/curve duct," Ph.D. thesis, Techinesche Universitaet Muenchen, Germany.

[13] McGrattan, K.B., Baum, H.R., Rehm, R.G., Hamins, A., and Forney, G.P., 1999, "Fire dynamics simulator: technical reference guide," National Institute of Standards and Technology (NIST).

[14] Peskin C.S. 1972, "Flow patterns around heart valves: a numerical method" J. of Computational Physics Vol. 10, pp 252-271.

[15] Goldstein D., Handler R. and Sivovich L. 1995, "Direct numerical simulation of turbulent flow over a modeled riblet covered surface" J. of Fluid Mech. **302** pp333-376.

[16] Restivo, A., 1979, "Turbulent flow in ventilated rooms", Ph.D.thesis, University of London, UK.

[17] Murakami, S., 1998, "Overview of turbulence models applied in CWE, 1997," J. of Wind Engineering and Industrial Aerodynamics, **74-76**, pp. 1-24.

[18] Cheesewright, R., King, K.J., and Ziai, S., 1986, "Experimental data for validation of computer codes for prediction of two-dimensional buoyant cavity flows", *ASME Winter Annual Meeting, HTD-60,* Anaheim, pp. 75-81.

[19] Wilcox, D.C., 1988, "*Turbulence modeling for CFD* (second edition)", DCW industries, La Canada, California.

[20]   Yuan, X., Chen, Q., Glicksman, L.R., Hu, Y., and Yang, X., 1999, "Measurements and computations of room airflow with displacement ventilation," ASHRAE Transactions, **105**(1), pp. 340-352.

[21]   Stolz, S. and Adams, N.A., 1999 "An approximate deconvolution procedure for large-eddy simulation", Physics of Fluids, Vol.11, no. 7, pp1699-1701.

Table 1. Computing time needed by different numerical schemes.

Computer	Alpha Workstation		Cray T90 (one Processor)	Cray T90 (14 Processors)
Time steps	100	250	60,000	
Grid number	130x34x34	130x34x34	130x34x34	130x34x34
Conventional iteration code	796 s	1800 s	160 h	
FFT code	240 s	600 s	16 h	1.5 h
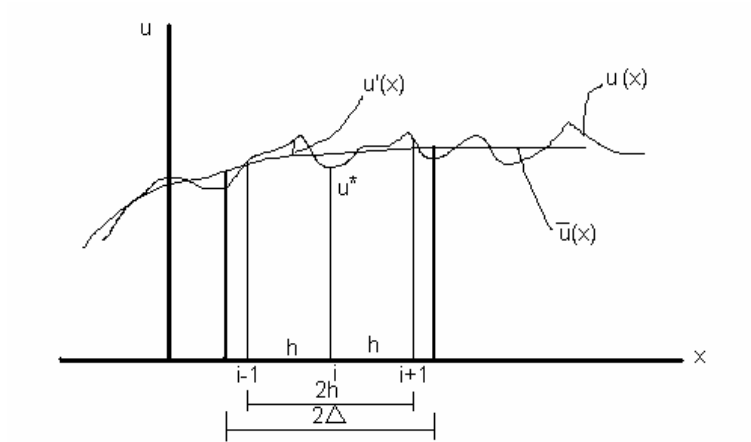
Figure 1.   Relationship between the filtered and unfiltered velocities.
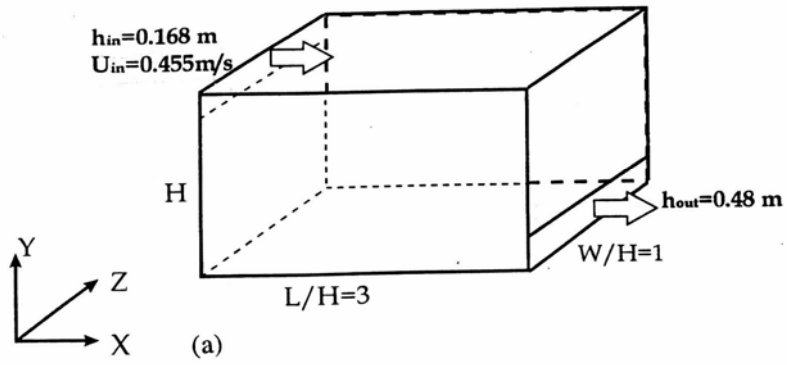
Figure 2. The schematic of the room with forced convection.
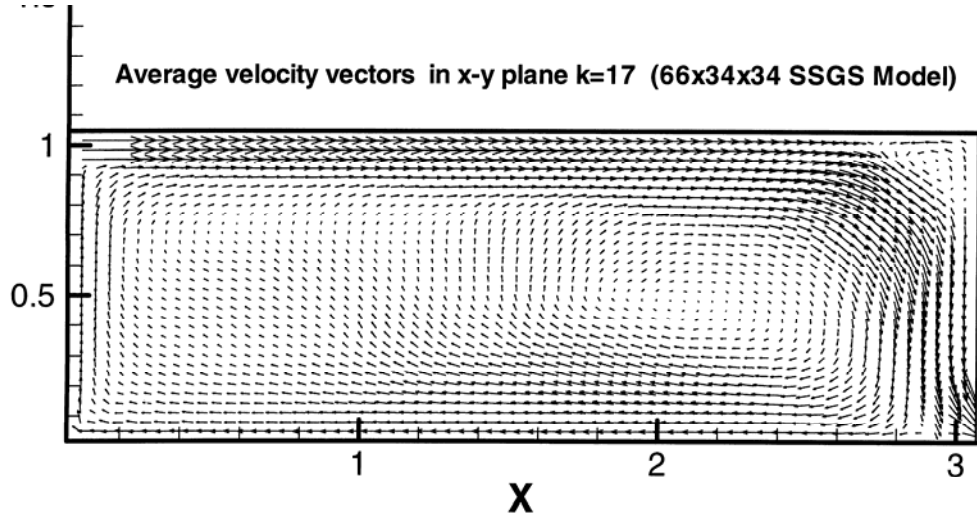
Figure3. Mean airflow pattern in the middle plane of the room.
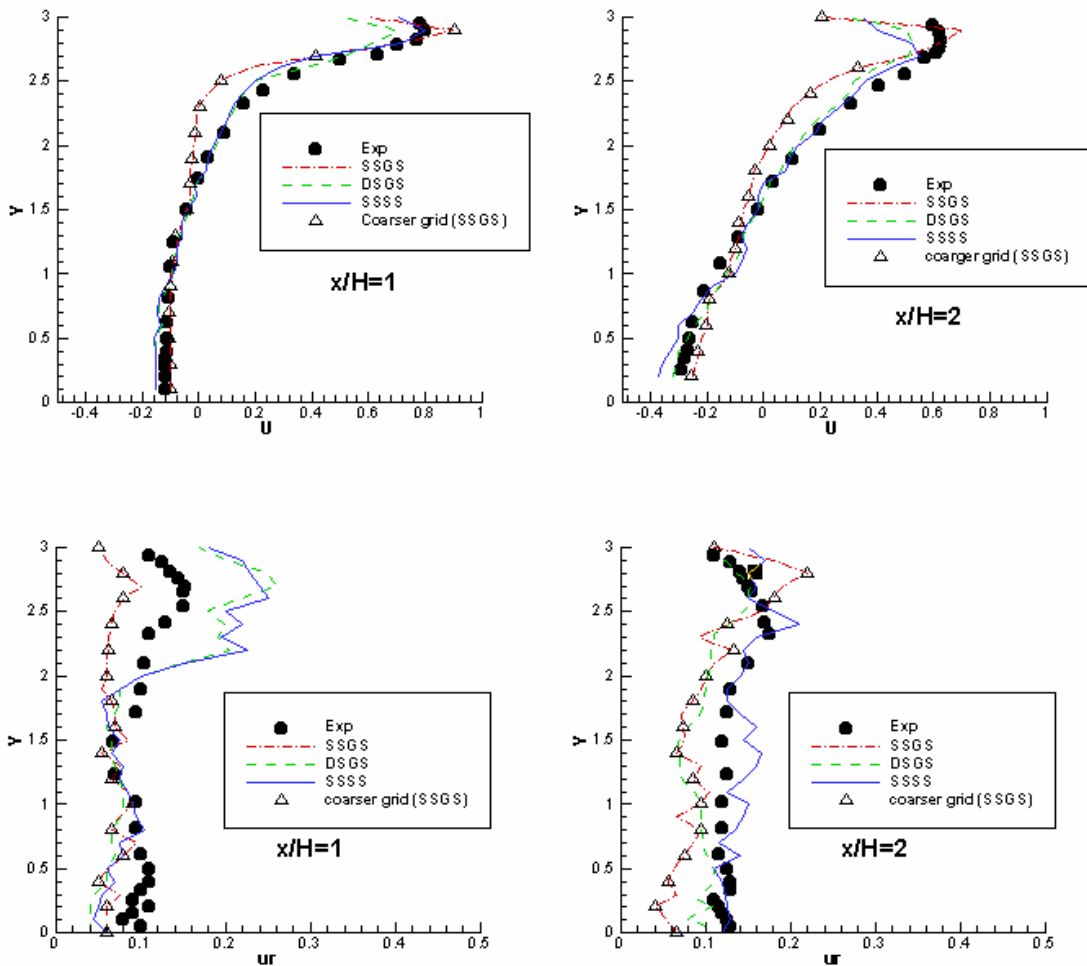
Figure 4. Comparison of the computed mean and fluctuation velocity profiles with the experimental data at x=H and 2H sections.
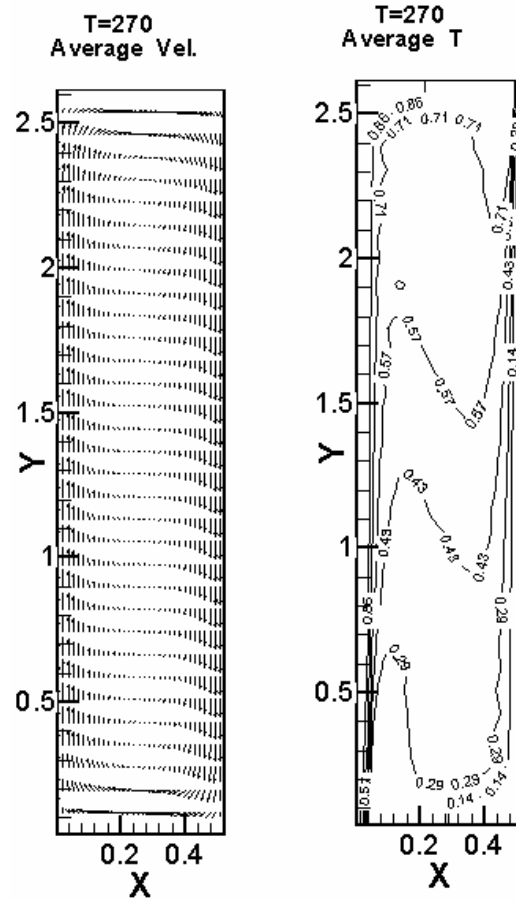
Figure 5. The mean airflow pattern and dimensionless air temperature distribution in the middle section of the cavity. ($T = \dfrac{t - t_c}{t_h - t_c}$, where t_h and t_c are the temperatures of the hot wall and cold wall, respectively).
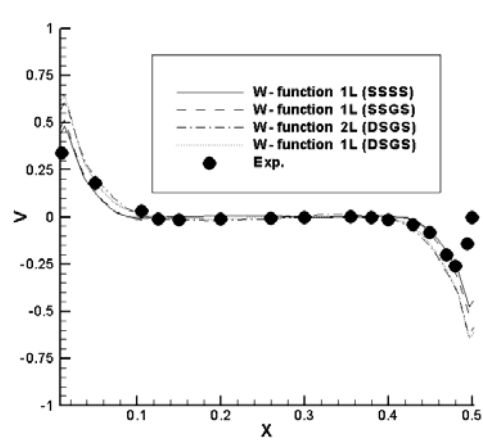
(a)
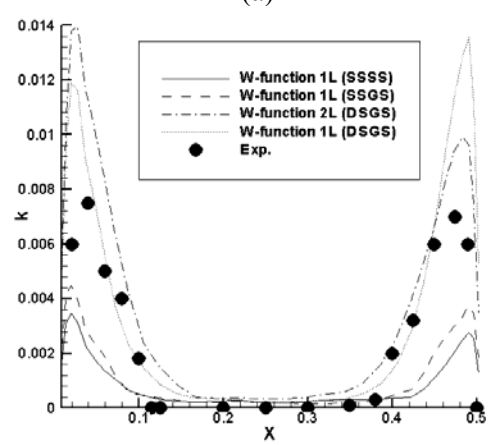
(b)
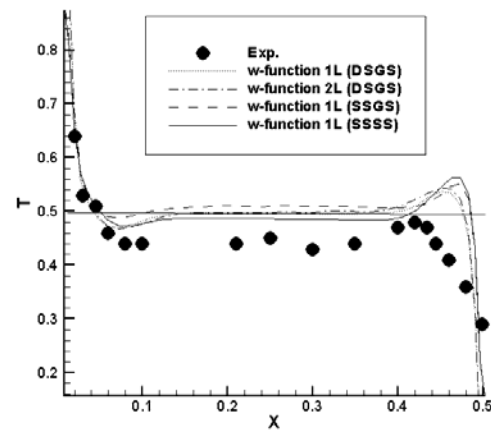
(c)

Figure 6. The computed mean profiles of (a) mean air velocity, (b) turbulent kinetic energy, and (c) dimensionless temperature in the mid-height of the cavity and the corresponding experimental data.
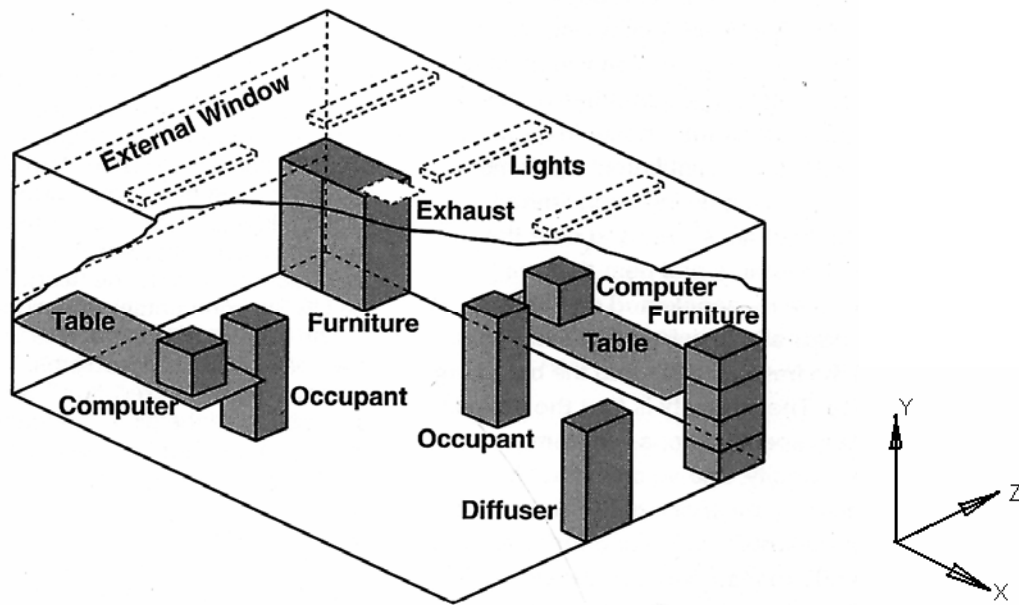
Figure 7. The schematic of a two-person office with displacement ventilation.
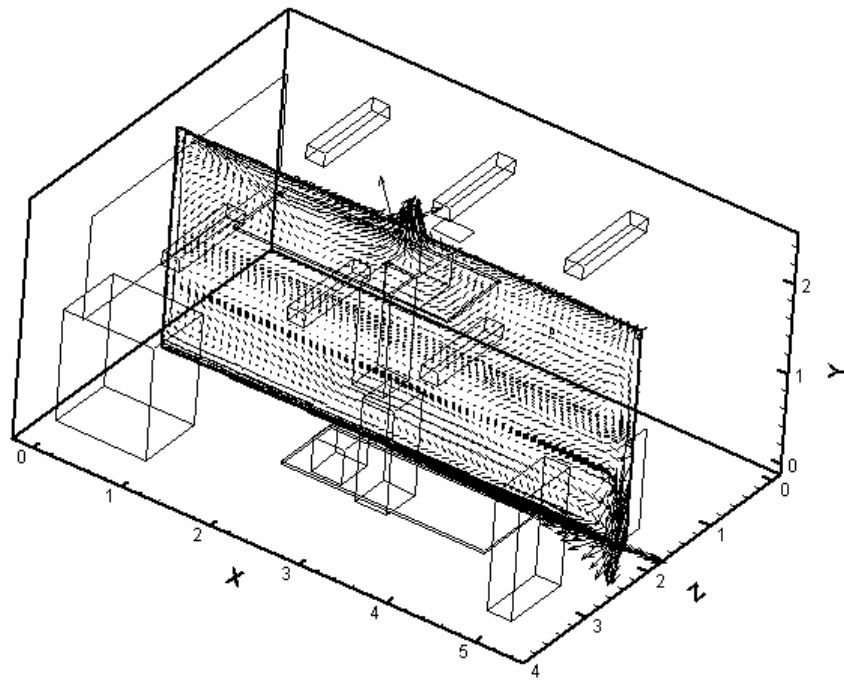
(a)
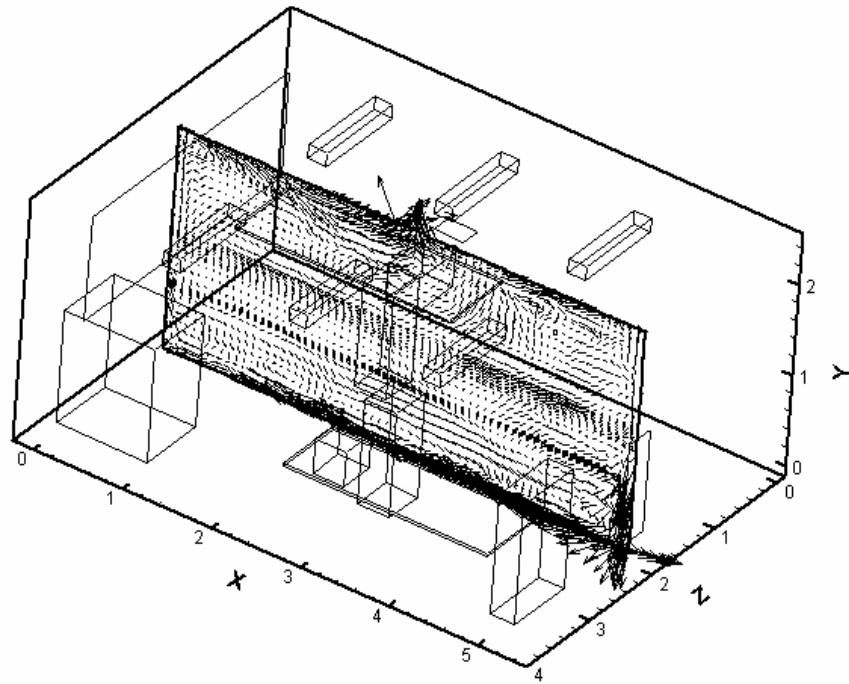
(b)

Figure 8. The (a) mean and (b) instantaneous airflow patterns in the middle section of the office.
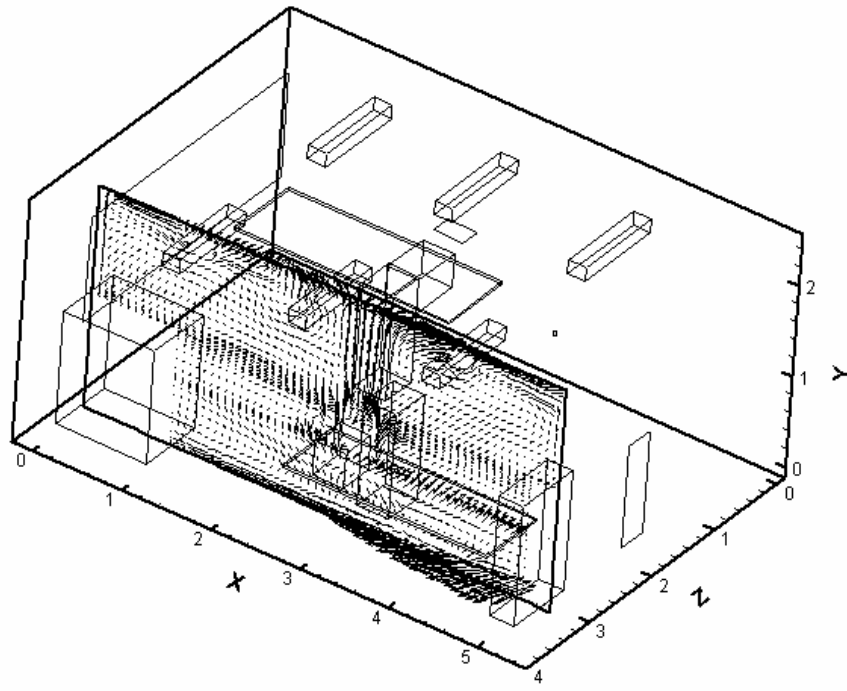
(a)
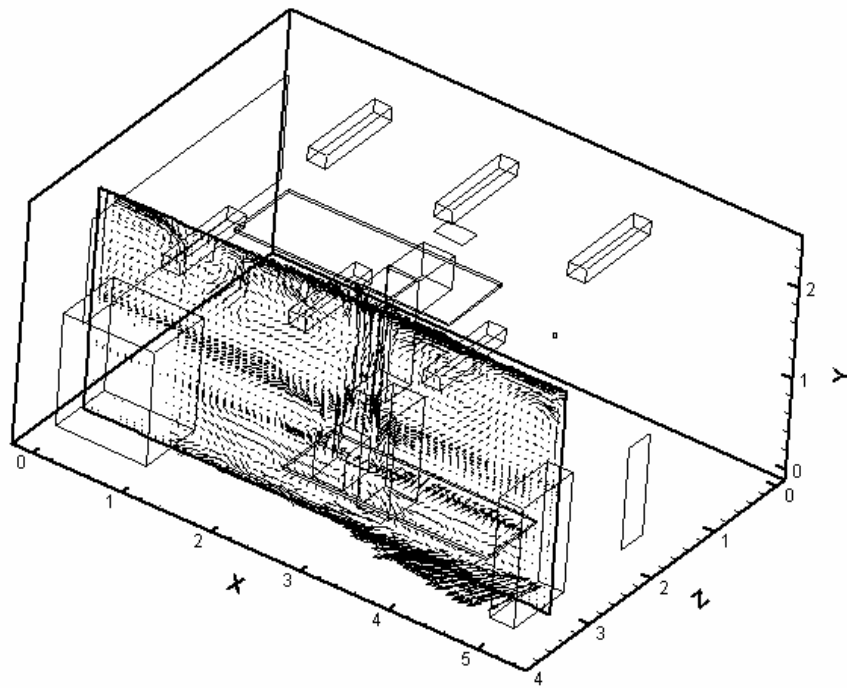
(b)

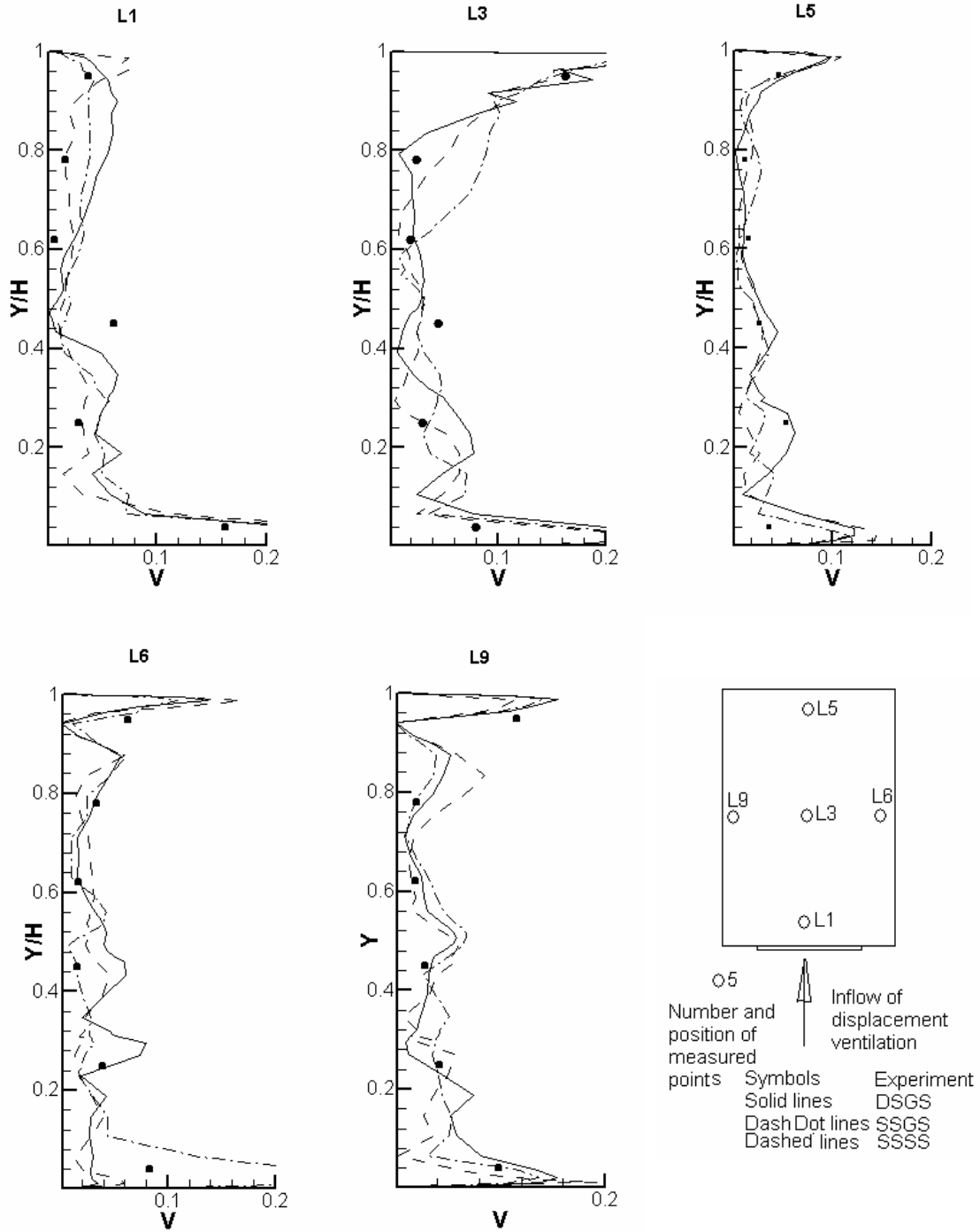Figure 9. The (a) mean and (b) instantaneous airflow patterns at the section near the side wall of the office.

Figure 10. Comparison of the computed mean air velocity profiles with the experimental data at five different locations in the room (m/s).
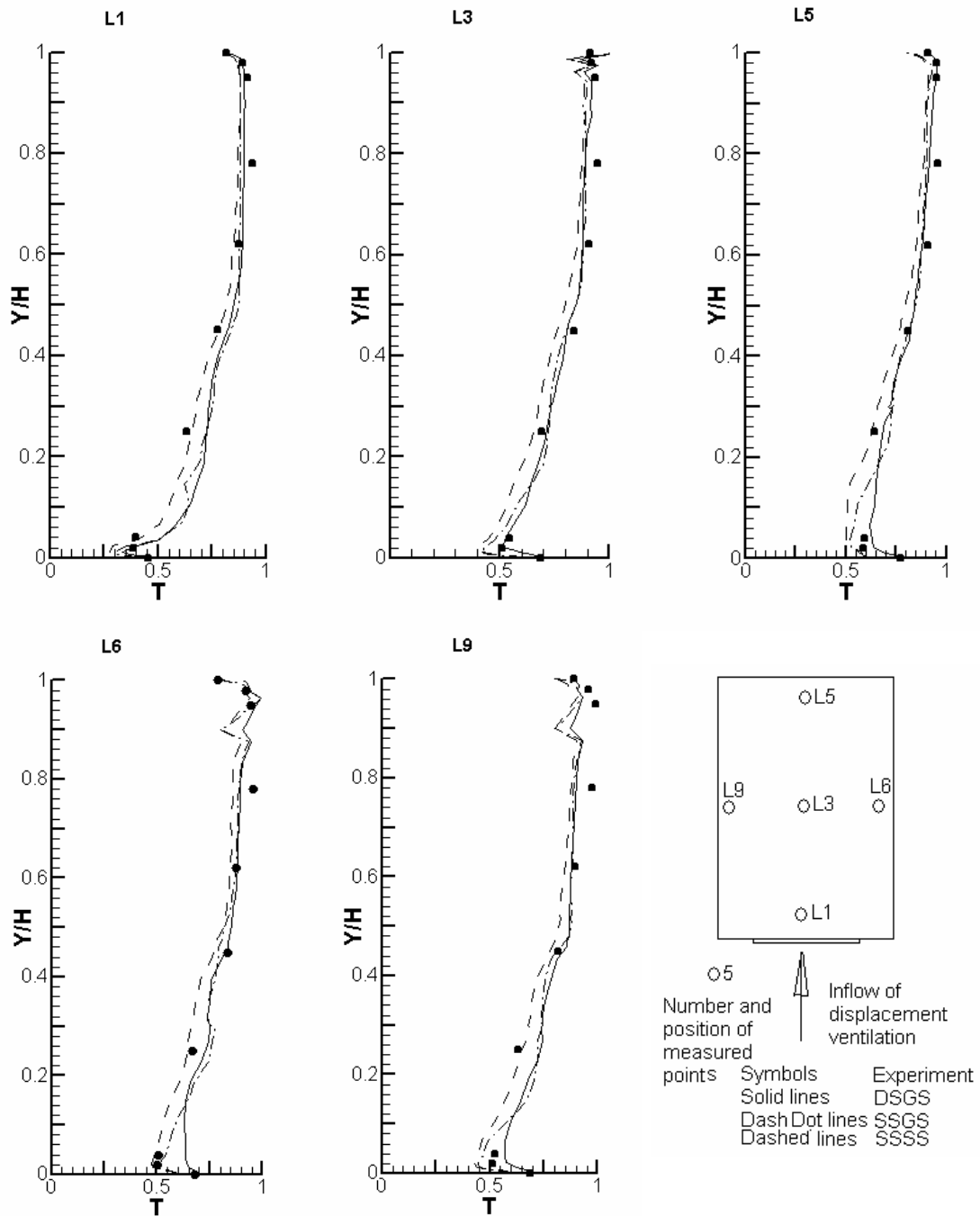
Figure 11. Comparison of the computed mean air temperature with the experimental data at five different locations in the room ($T = \dfrac{t - t_s}{t_{exh} - t_s}$, t_s=17.0°C, t_{exh}=26.7°C, where t_s and t_{exh} are the temperatures of the supply and exhaust, respectively).
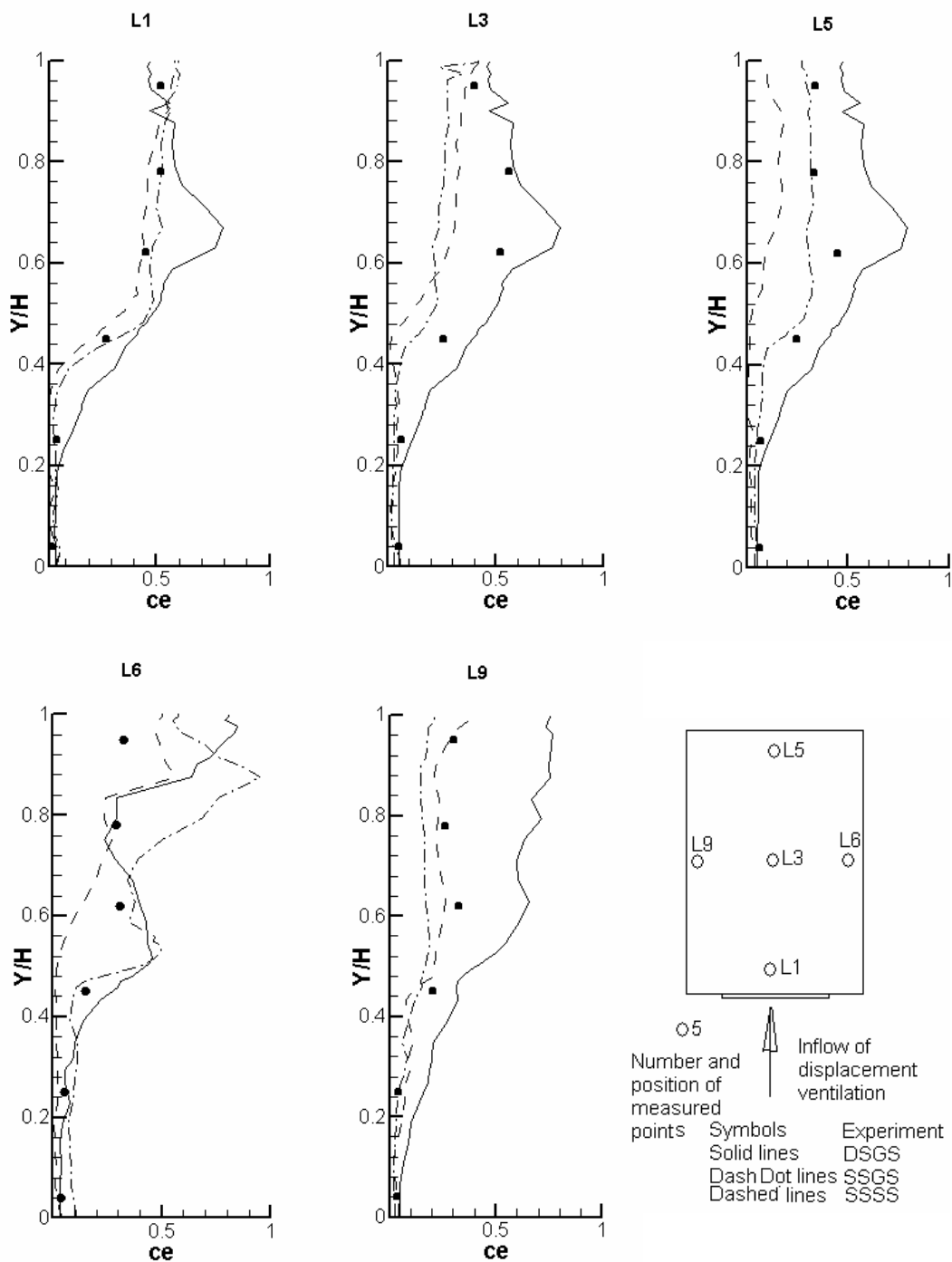
Figure 12. Comparison of the computed mean tracer-gas (SF_6) concentration distributions with the experimental data at different locations in the room ($ce=(c-c_s)/(c_e-c_s)$, $c_e=0$ ppm, $c_s=0.42$ ppm, where c_s and c_e are the tracer gas concentrations of the source and environment, respectively).